

Analytical Extraction of Plasma Properties Using a Hall Thruster Efficiency Architecture

IEPC-2007-188

*Presented at the 30th International Electric Propulsion Conference, Florence, Italy
September 17-20, 2007*

Daniel L. Brown[Ⓜ], C. William Larson^Σ, James M. Haas[§]
Air Force Research Laboratory, Edwards AFB, CA, 93524, USA

and

Alec D. Gallimore^α
*Plasmadynamics and Electric Propulsion Laboratory
University of Michigan, Ann Arbor, MI, 48109, USA*

Abstract: An investigation of the conversion from anode electrical energy to jet kinetic energy in a laboratory model Hall thruster yielded an experimentally determined thrust efficiency that was analytically decomposed into the product of propellant, voltage, and current utilization efficiency. This method accounts for loss of propellant utilization from plume divergence, unionized propellant, and multiply charged ions. Current and voltage utilization losses include recycled electrons used for ionization processes and the fractional loss of acceleration voltage within the discharge chamber. The architecture of the efficiency analysis is such that energy efficiency becomes naturally expressed as a product of voltage and current utilization efficiencies, and is rigorously separated from propellant utilization efficiency. A systematic investigation of thruster performance and the far-field plume provided insight into the loss mechanisms and plasma properties from 100 to 400 V discharge for constant mass flow rate (20 mg/s) and constant power operation (6 kW). Experimental parameter groups were calculated based on the measured thrust and telemetry data. When interpreted with measured ion beam current and most probable ion voltage, the efficiency analysis enabled several plasma parameters to be deciphered, including: average ion charge, ionization mass fraction, and momentum beam divergence half-angle. The following study creates an analytical procedure for extracting plasma parameters based on macroscopic performance and plume measurements, and enables the interpretation of limits for consistent sets of allowable discharge properties.

DISTRIBUTION STATEMENT A. Approved for public release; distribution is unlimited.

[Ⓜ] Research Scientist, ERC Inc.; Ph.D. candidate, University of Michigan: Daniel.Brown@edwards.af.mil

^Σ Research Scientist, Spacecraft Propulsion Branch: Carl.Larson@edwards.af.mil

[§] Group Lead, Spacecraft Propulsion Branch: James.Haas@edwards.af.mil

^α Professor and Laboratory Director, Department of Aerospace Engineering; Associate Dean, Horace H. Rackham School of Graduate Studies: Alec.Gallimore@umich.edu

Nomenclature

a	= ‘quality’ indicator of ionization in the Φ_{VDF} contribution of the Φ -Factor, $a \approx 0.99$
E_1	= first experimental parameter group = $\frac{1}{2}(\mathbf{T}/\dot{m})^2/(V_a \mathcal{F}/\mathcal{M}) = \Phi(1-\beta)\chi$.
E_2	= second experimental parameter group = $(\dot{m}/I_a)(\mathcal{F}/\mathcal{M}) = (1-r)/\chi$.
\mathcal{F}	= Faraday constant, 96,485 coulombs/mol of charge.
f_i	= ion mass fraction at exit = $f_1+f_2+f_3$.
f_1^*, f_2^*, f_3^*	= reduced ion mass fractions at exit, $f_1^*+f_2^*+f_3^*=1$, $f_1/f_i = f_1^*$.
g_0	= Earth’s gravitational constant at sea level, 9.806 m/s ² .
I_a	= measured anode current.
I_{sp}	= specific impulse, independent of unit system, $I_{\text{sp}} = \langle \mathbf{v} \rangle / g_0$.
\dot{m}	= measured propellant anode mass flow rate.
\dot{m}_c	= measured propellant cathode mass flow rate.
\mathcal{M}	= molecular weight of propellant, xenon = 0.1313 kg/mol.
P_{in}	= input power to anode.
P_{jet}	= power of jet = $\frac{1}{2} \dot{m} \langle \mathbf{v}^2 \rangle$.
P_{magnets}	= input power to electromagnets.
Q	= average charge of xenon ions, $f_1^* + 2f_2^* + 3f_3^*$.
q	= unit of charge, 1.609×10^{-19} C.
r	= fractional loss of current, electron recycle fraction.
$(1-r)$	= fractional ion beam current, current utilization efficiency.
\mathbf{T}	= measured thrust vector.
V_a	= measured anode voltage.
$\langle \mathbf{v} \rangle$	= mass weighted average exit velocity, specific impulse.
$\langle \mathbf{v}^2 \rangle$	= mass weighted average squared exit velocity.
$\langle \mathbf{v}^2 \rangle_+$	= mass weighted average squared ion exit velocity.
α	= plume momentum divergence half-angle.
β	= fractional loss of acceleration voltage.
$(1-\beta)$	= voltage utilization efficiency.
ΔV	= average ion acceleration voltage = $(f_1^* \delta V_1 + 2f_2^* \delta V_2 + 3f_3^* \delta V_3) / Q$.
$\delta V_1, \delta V_2, \delta V_3$	= acceleration voltages of $\text{Xe}^{+1}, \text{Xe}^{+2}, \text{Xe}^{+3}$.
η_{energy}	= energy efficiency = $P_{\text{jet}}/P_{\text{in}}$.
η_{thrust}	= experimental thrust efficiency.
η_{total}	= total thruster efficiency = $\eta_{\text{thrust}} [\dot{m} / (\dot{m} + \dot{m}_c)] [P_{\text{in}} / (P_{\text{in}} + P_{\text{magnets}})]$
Φ	= Φ -Factor = $\Phi_{\text{VDF}} \Phi_{\text{DIV}} = \langle \mathbf{v} \rangle^2 / \langle \mathbf{v}^2 \rangle$, propellant utilization efficiency.
Φ_{VDF}	= velocity distribution component of the Φ -Factor, = $a f_i$
χ	= χ -Factor = $f_i Q$, average charge per particle (ions and neutrals), beam current per mol of propellant.

I. Introduction

HALL thrusters utilize orthogonal electric and magnetic fields to electrostatically accelerate ions through a discharge channel, while recycled electrons travel in an azimuthal trajectory around the channel annulus with a small axial velocity component leading to the anode. Complex coupling of plasma properties and perturbation effects make physical parameters such as momentum beam divergence, ionization fraction, and average ion charge difficult to measure directly. However, these values can be analyzed using thrust and far-field plume measurements. An investigation of thruster operation for constant anode flow operation (20 mg/s) and constant power operation (6 kW) is examined to demonstrate the utility of thruster utilization efficiencies and the efficacy in bounding a consistent set of plasma properties from a limited number of macroscopic measurements.

II. Hall Thruster Efficiency Analysis

A Hall thruster efficiency architecture developed at AFRL analytically separates thruster efficiency into the product of three utilization efficiencies: voltage, current, and propellant utilization efficiency. This method

accounts for the effects of the ion velocity distribution function (VDF), ionization fraction, multiply charged ion species, electron recycle fraction, momentum plume divergence, and the loss of acceleration voltage within the discharge chamber. The architecture is formulated such that energy efficiency becomes naturally expressed as a product of voltage and current utilization efficiencies, and is rigorously separated from propellant utilization efficiency. Thus, thrust efficiency is the product of propellant utilization efficiency and energy efficiency. A detailed account of the following efficiency architecture with a comprehensive examination of Hall thruster physics and its manifestation in thruster utilization efficiencies is detailed in the work of Larson, Brown, and Hargus.¹ The voltage and current utilization efficiencies are analogous to those in the efficiency analysis by Hofer and Gallimore.² However, the propellant utilization in this study accounts for neutrals in the propellant utilization efficiency. Contrary to previous phenomenological efficiency studies, the utilization efficiencies in the following architecture are analytically decomposed from thrust efficiency, which allows for the extraction of additional plasma parameters from a small number of experimental measurements.

Hall thruster efficiency is defined as the conversion of anode electrical energy to directed momentum to produce thrust, and experimentally determined as:

$$\eta_{\text{thrust}} = \frac{\frac{1}{2} \dot{m} \langle v \rangle^2}{P_{\text{in}}} = \frac{1}{2} \left(\frac{T}{P_{\text{in}}} \right) \langle v \rangle \quad (1)$$

In Eq. (1), thrust efficiency may also be written as the product of the thrust-to-power ratio (T/P_{in}) and $\langle v \rangle$, where $\langle v \rangle$ is the propellant jet specific impulse (impulse per unit mass) with dimensions of velocity in SI units. This expression reveals the trade-off between T/P_{in} and specific impulse for a given thruster efficiency, and explicitly shows that increasing specific impulse to high values at constant efficiency requires diminishing thrust and/or increasing power. Further analysis of the thrust efficiency provides insight into losses in Hall thruster performance.

$$\eta_{\text{thrust}} = \frac{\langle v \rangle^2}{\langle v^2 \rangle} * \frac{\frac{1}{2} \dot{m} \langle v^2 \rangle}{I_a V_a} = \Phi \frac{P_{\text{jet}}}{P_{\text{in}}} = \Phi \eta_{\text{energy}} \quad (2)$$

where

$$\Phi = \frac{\langle v \rangle^2}{\langle v^2 \rangle} \quad (3)$$

The derivation in Eq. (2) separates thrust efficiency into the product of energy efficiency and the Φ -Factor. Energy efficiency is the ratio of jet kinetic energy to anode electrical energy. The Φ -Factor defined in Eq. (3) represents propellant utilization: it is unity for 100% ionization to a single ion species where all thrust vectors are directed along the same axis. It is a direct relation between the ion momentum and kinetic energy, which accounts for losses due to incomplete ionization, plume divergence and non-uniformity of the VDF that occurs when the jet is composed of multiple ion species with varying velocities.

Energy efficiency can be further divided into the product of voltage and current utilization. The χ -factor is introduced in Eq. (4) to account for the average particle charge of propellant in the plasma, including unionized neutral propellant. It is defined as the product of particle ionization fraction, f_i , and average ion charge, Q , in Eq. (5) for a plasma with three ion species.

$$\eta_{\text{energy}} = \frac{\frac{1}{2} \dot{m} \langle v^2 \rangle}{P_{\text{in}}} = \frac{\langle v^2 \rangle}{\langle v^2 \rangle_+} \frac{\frac{1}{2} \langle v^2 \rangle_+}{\frac{\mathcal{F}}{\mathcal{M}} V_a} * \frac{\dot{m} \mathcal{F}}{I_a \mathcal{M}} = \chi(1-\beta) \frac{(1-r)}{\chi} = (1-\beta)(1-r) \quad (4)$$

where

$$\chi = f_i (f_1^* + 2f_2^* + 3f_3^*) = f_i Q \quad (5)$$

Although the χ -factor cancels in the energy efficiency term, it reveals the physical nature of the voltage and current utilization inherent in the thrust efficiency. The voltage utilization, $(1-\beta)$, shown in Eq. (6) compares the average potential energy gained by ions with the total potential available from the anode discharge voltage.

$$\frac{\langle v^2 \rangle}{\langle v^2 \rangle_+} \frac{\frac{1}{2} \langle v^2 \rangle_+}{\frac{\mathcal{F}}{\mathcal{M}} V_a} = f_i \left(f_1^* \frac{\partial V_1}{\partial V_a} + 2f_2^* \frac{\partial V_2}{\partial V_a} + 3f_3^* \frac{\partial V_3}{\partial V_a} \right) = f_i \frac{\Delta V}{V_a} (f_1^* + 2f_2^* + 3f_3^*) = f_i (1-\beta) Q \quad (6)$$

To simplify the analysis, all ions are assumed to be created at the same location. Thus, the potential available for acceleration is ΔV and the voltage utilization efficiency is $(1-\beta) = \Delta V/V_a$. This utilization is calculated from the most probable ion voltage with an RPA. An ExB measurement would provide reduced ion mass fractions, and enable a voltage utilization to be calculated for each ion species. Voltage utilization is maximized for complete ionization at the anode face. The approximation used in Eq. (6), in which average neutral to ion specific kinetic energy is equal to f_i (i.e., $\langle v^2 \rangle / \langle v^2 \rangle_+ \approx f_i$), is accurate to better than 99.999%. This calculation is based on the velocity ratio of singly charged xenon ions to unionized neutral propellant being greater than or equally to 100, which was experimentally determined using electrostatic probes by Hargus, Meezan, and Cappelli for a low power Hall Thruster.³

The total ion beam current exiting the thruster is given by $[\chi \dot{m} (\mathcal{F}/\mathcal{M})]$. The ratio of ion beam current to the discharge current is the current utilization efficiency $(1-r)$, as defined in Eq. (7). The quantity 'r' is the electron recycle fraction, and represents the electrons emitted from the cathode that are not used for beam neutralization.

$$(1-r) = \frac{\dot{m} \mathcal{F}}{I_a \mathcal{M}} \chi = \frac{\dot{m} \mathcal{F}}{I_a \mathcal{M}} f_i (f_1^* + 2f_2^* + 3f_3^*) \quad (7)$$

Current utilization approaches unity as the number of recycled electrons approaches zero. However, there is a minimum value of 'r' required to sustain ionization processes in the thruster and provide the energy necessary for a given ionization fraction and ion species distribution.

Two experimental parameter groups, E_1 and E_2 , may be written using the preceding utilization efficiencies. These parameters are calculated based solely on thruster telemetry and performance measurements, and provide insight about the relative magnitudes of the individual utilization efficiencies. The product of E_1 and E_2 is equal to thruster efficiency as shown in Eq. (8).

$$\eta_{\text{thrust}} = \Phi(1-\beta)(1-r) = [\Phi(1-\beta)\chi] \left[\frac{(1-r)}{\chi} \right] = E_1 E_2 \quad (8)$$

Equations (9) and (10) define how E_1 and E_2 depend on the utilization efficiencies. The quantity E_1 is a function of propellant utilization, voltage utilization, and the χ -factor. It is important to note that since both the χ -factor and Φ -Factor are directly proportional to the ionization fraction, the experimental parameter E_1 is proportional to f_i^2 . Since the quantity E_2 is inversely proportional to f_i , it is expected that E_1 will be more sensitive to changes in the ionization fraction.

$$E_1 = \Phi(1-\beta)\chi = \Phi_{\text{DIV}} (1-\beta) a Q f_i^2 = \frac{1}{2} \frac{\left[\frac{\mathbf{T}}{\dot{m}} \right]^2}{V_a \frac{\mathcal{F}}{\mathcal{M}}} \quad (9)$$

$$E_2 = \frac{(1-r)}{\chi} = \frac{(1-r)}{f_i Q} = \frac{\dot{m}}{I_a} \frac{\mathcal{F}}{\mathcal{M}} \quad (10)$$

In the absence of diagnostics for the determination of plasma properties, these experimental parameter groups allow limits to be placed on acceptable values for the average charge Q , ionization fraction f_i , and momentum divergence half-angle, α . Analysis using E_1 will ignore variations in the quality term 'a' from Eq. (9), since this term is approximately 0.98 for modern laboratory model Hall thrusters and rarely deviates more than 2% from unity. A full explanation is found elsewhere in the literature.¹

III. Experimental Apparatus

A. AFRL Test Facilities

Performance verification tests at AFRL were conducted in Chamber 3, a stainless steel, cylindrical vacuum chamber 3.3 m diameter by 8-m long. The thruster exit plane is located in the center of the chamber diameter, pointing down the long axis approximately 7 m from the far end. All surfaces that are optically visible to the plasma plume are shielded with 1/2" thick, high purity, sulfur-free carbon plates. A dedicated dry Stokes mechanical pump reaches rough vacuum with a pumping speed of 450 L/s and a Pfeiffer Vacuum turbomolecular pump removes lighter gases. The facility utilizes eight helium-cooled cryopanel, resulting in a maximum xenon pumping speed of 140,000 L/s. The heat load to these cryopanel is moderated by shrouds coated with low emissivity paint, which are cooled by four IGC Polycold Cryogenic Refrigeration units. A conservative measurement of the ultimate base pressure is less than 1×10^{-7} torr.

An MKS Instruments cold cathode ionization gauge, located on the chamber ceiling above the thruster, registered background pressure. Using a xenon calibration factor of 2.87, the adjusted pressure for flow rates of 10, 15, and 20 mg/s were 8×10^{-6} , 1.3×10^{-5} , 1.5×10^{-5} Torr. High background pressure artificially raises performance due to ingestion of background neutrals into the discharge chamber. Randolph's criterion asserts that facility effects have negligible influence on performance for background pressures below 2×10^{-5} Torr.⁴ Since all performance measurements were taken at pressures below this threshold, it was determined that neutral entrainment at these pressure and flow rates had a negligible impact on thruster performance.^{5,6} No corrections to performance measurements were made to compensate for facility effects.

The propellant flow system was supplied with research grade xenon (99.999% purity) via 1/4 inch stainless steel tubing. Anode flow was controlled with a 1000 sccm Unit 1661 digital mass flow controller. Cathode flow was regulated with a 50 sccm Unit 7300 digital mass flow controller. All mass flow controllers were calibrated with xenon prior to testing with a DH Instruments Molbloc/Molbox gas flow calibration system with an estimated uncertainty of $\pm 0.5\%$ according to the manufacturer's specifications.

Thruster discharge power was provided by two Electronic Measurement Inc. ESS Power Supplies arranged in parallel, each capable of 600V, 16A output. A simple RLC circuit provided low pass filtering of the main discharge, and the thruster body was connected to chamber ground. Discharge voltage, discharge current, and cathode potential were monitored through high accuracy current shunts with an uncertainty of $\pm 0.5\%$. Coils were energized with Sorenson DLM 60-10 power supplies. The cathode heater was powered with an EMS 20-30 supply and the cathode keeper used a Sorenson LHP 300-3.5 power supply. The heater power supply was shut down during thruster operation.

Thrust measurements were taken with a null type, inverted pendulum thrust stand. At steady state conditions, thrust measurements varied by < 0.5 mN. A diluted Glycol solution at 10°C cooled the copper shroud surrounding the thrust stand to decrease thermal drift. Thrust stand calibrations were performed in several configurations to test the influence of electromagnet coils and cathode operation. Repeated tests showed consistent thruster performance to within 1%, signifying that the calibrations and zero offsets were unaffected by these variables. As the thrust stand and thruster reached thermal equilibrium, the calibration curves showed repeatability with less than 1% variation. The zero offset was recorded after each test point and used with the calibration slope to calculate thrust. In cases where the thrust stand was not calibrated after each operating condition, the zero position was found for each point from a linear interpolation of the zero offset before firing and after shutdown. Inclination was managed with a stepper motor to level the thruster and minimize null coil current during high thrust operation. This minimized thermal drift in the null coil signal after shutdown and yielded a more reliable zero offset. Due to the highly repeatable thrust measurements and minimal thermal drift, uncertainty in thrust is estimated at $\pm 1\%$.

A 22-bit Agilent Datalogger transmitted thrust, mass flow, and power to a LabView code monitoring the anode efficiency and thruster performance in real-time. For a given discharge voltage and flow rate, the coil currents were adjusted for maximum anode thruster efficiency. When peak efficiency was achieved, the magnet coils were further tuned for maximum T/P ratio. The efficiency optimization did not always correspond to minimum discharge current, since decreasing thrust would further reduce anode thruster efficiency (Efficiency \sim Thrust² / Current).

B. Hall Thruster

A 6 kW laboratory model test-bed Hall thruster was used in this investigation. A thruster with large channel diameter enabled the placement of a centrally mounted internal cathode that was directed along the thruster centerline. The schematic in Fig. 1 illustrates the internal cathode configuration in a typical Hall thruster design. The thruster utilizes inner and outer electromagnets to form standard magnetic lens topography.⁸ Constant anode propellant flow operating conditions at 20 mg/s ranged from 100 – 400 V discharge. Constant power operating conditions at 6 kW ranged from 200 – 400 V. Cathode flow fraction was 7% at all operating points.

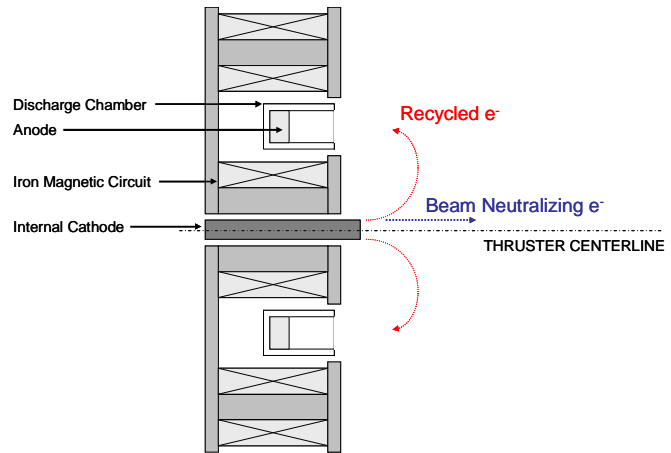


Figure 1. Schematic of a centrally mounted internal cathode configuration in a typical Hall thruster design.

C. Plasma Diagnostics

Plume examinations were executed one meter downstream of the thruster exit plane as a function of angular position from centerline. The plasma diagnostic array at AFRL, shown in Fig. 2, includes a retarding potential analyzer (RPA), Langmuir probe, gridded Faraday probe, and nude Faraday probe. A rotational arm with axis of rotation located above the exit plane on thruster centerline is controlled with a Thermionics Stepping Motor Controller. The probe array, as shown in Figure 3, is swept continuously 180 degrees in a constant one meter radius arc for Faraday probe measurements. The continuous rotational motion at low speeds minimizes mechanical arm vibration and prolongs probe life by decreasing time in the plume. RPA and Langmuir probe data collection is taken on thruster centerline one meter downstream of the exit plane, with the Langmuir probe 3 cm off axis.



Figure 2. Plasma diagnostic array at AFRL. Probes from left to right include: Langmuir probe, RPA, nude Faraday probe, and gridded Faraday probe.

1. Retarding Potential Analyzer

An RPA measured the ion voltage distribution on the thruster centerline with a series of positively and negatively biased retarding grids. The positive potential of an ion retarding grid acts as a high pass filter, and only permits ions above the grid threshold voltage to reach the collector. The resulting ion voltage distribution is found from the derivative of the current-voltage relationship.⁷

A series of grids, as shown in Figure 4, filters ambient electrons and selected ions before they reach the copper collector. Grids are composed of

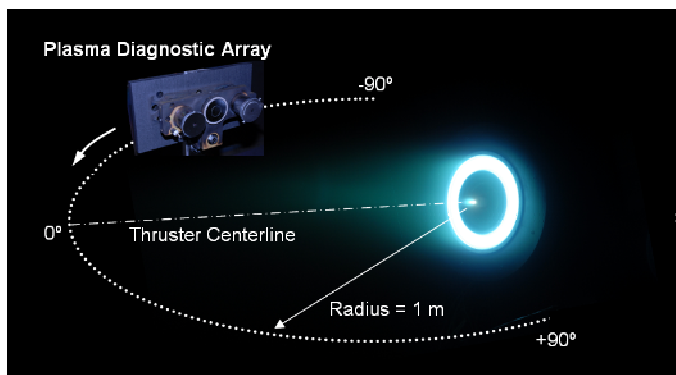


Figure 3. Plasma diagnostic array on the rotational arm at AFRL.

a 0.005" thick, photochemically etched 316 SS with an open area fraction of approximately 38% and separated by MACOR spacers. A phenolic sleeve inside the stainless steel body electrically isolates the grids. A ceramic cover with a 1 cm diameter opening reduced the ion flux at high flow rates and avoided current saturation of the collector electronics. The outer grid exposed to the plume is floating to minimize the perturbation between the probe and ambient plasma. Electron repelling grids 2 and 4 are biased to -15 V below thruster ground by a BK Precision 1760 Triple Output DC power supply. Grid 2 repels electrons from the plume while grid 4 suppresses secondary electrons resulting from ion impacts with the collector. The ion retarding grid is connected to a Keithley 2410 1100 V Sourcemeter and swept from 0 to ~500 V with respect to ground. A picoammeter reads the collection current, which is recorded as a function of voltage applied to the ion repelling grid. Further RPA construction and operation details may found elsewhere in electric propulsion literature.^{8,9}

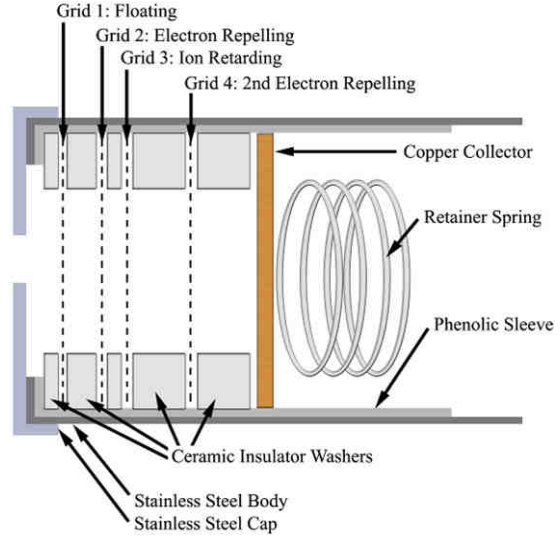


Figure 4. Cross-sectional schematic of the RPA showing ion and electron repelling grids.

2. Langmuir Probe

A single, cylindrical Langmuir probe parallel to the centerline plume was used to measure plasma potential. The probe consisted of a 0.2 mm diameter, 15 mm long Tungsten wire connected to a Keithley 2400 Sourcemeter. Langmuir probe data were collected during the RPA sweep and analyzed to determine the plasma potential for RPA voltage distribution calculations. The Langmuir probe was positioned 3 cm and approximately 1 degree off the centerline axis. Prior studies concluded the difference in plasma potential varied by only a few volts across large angles.¹⁰ Due to the proximity of the Langmuir probe to the RPA, the difference in plasma potential between the diagnostics was estimated at less than one volt.

A potential diagram outlining the correlation between measured values with the most probable ion voltage and loss voltage is shown in Fig. 5. The average acceleration potential, ΔV , is found in Eq. (11) as the difference between the most-probable ion voltage from RPA traces (V_{RPA}) and plasma potential (V_{Plasma}). The loss voltage (V_{Loss}) in Eq. (12) is subsequently calculated from the difference between discharge voltage (V_a) and average acceleration potential. Voltage utilization efficiency can then be determined from the average acceleration voltage as shown in Eq. (13).

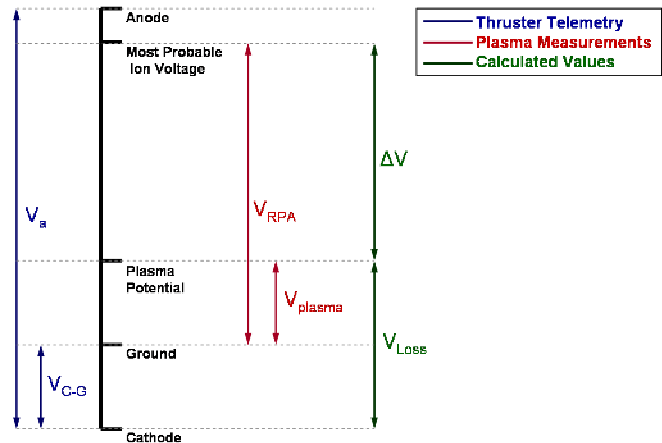


Figure 5. Potential diagram illustrating the relationship between measured voltages (V_a , V_{C-G}), plume measurements (V_{RPA} , V_{Plasma}) and calculated potentials (ΔV , V_{Loss}).

$$\Delta V = V_{RPA} - V_{Plasma} = V_a - V_{Loss} \quad (11)$$

$$V_{Loss} = V_a - \Delta V \quad (12)$$

$$(1 - \beta) = \frac{\Delta V}{V_a} = 1 - \frac{V_{Loss}}{V_a} \quad (13)$$

3. Nude Faraday Probe

The nude Faraday probe measured directed ion flux to a 19 mm collector electrode bordered by a 43 mm diameter annular guard ring. This guard ring is biased to the same negative potential as the collector and forms a uniform, planar sheath in front of the collection area. A simplified circuit diagram is shown in Fig. 6. The bias voltage is set to -15 V with respect to ground by a Sorenson LT 30-3 DC power supply. Collected current is found from the voltage drop across a 40.4 ohm shunt resistor, and corresponding current density is calculated from measured current divided by the collector electrode surface area.

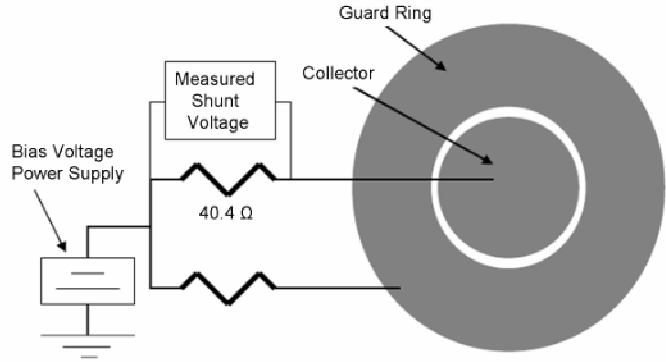


Figure 6. Simplified circuit diagram of the nude Faraday probe.

The 95% charge divergence half-angle (α_{95}) was calculated separately for left and right sides of the plume, and determined the location where the signal integrated to 95% of the total collected voltage from centerline to ± 90 degrees, as shown in Eq. (14). Charge divergence half-angle is generally larger than the momentum divergence half-angle extracted in the efficiency architecture. This effect is due to the presence of low energy ions on the wings, which artificially increase the collected current at large angles off thruster centerline.

$$0.95 \int_0^{\pm 90} j(\theta) \sin(\theta) d\theta = \int_0^{\pm \alpha_{95}} j(\theta) \sin(\theta) d\theta \quad (14)$$

Beam current is calculated by integrating current density in the hemisphere about thruster centerline as shown in Eq. (15). The ratio of calculated ion beam current to the discharge current provides the current utilization efficiency, (1-r).

$$I_{Beam} = 2\pi R^2 \int_0^{\pm 90} j(\theta) \sin(\theta) d\theta \quad (15)$$

Previous studies found plume measurements had a strong dependence on facility backpressure, resulting in an artificial increase in current density at half-angles approximately 30 degrees beyond thruster centerline. This dependence is attributed to the presence of charge exchange (CEX) ions, which account for a significant fraction of ions on the outer edges of the plume.^{11,12,13,14} Current collected on the outer wings is erroneously high and results in overestimation of the total ion beam current and charge divergence angles. Fig. 7 illustrates increased current density on the wings for a one meter radial sweep. A corrected nude Faraday probe current density is found from the linear extrapolation on a log scale for angles greater than 30 degrees off centerline.¹⁵ All calculations using current density from the nude Faraday probe use corrected values beyond 30 degrees off thruster centerline.

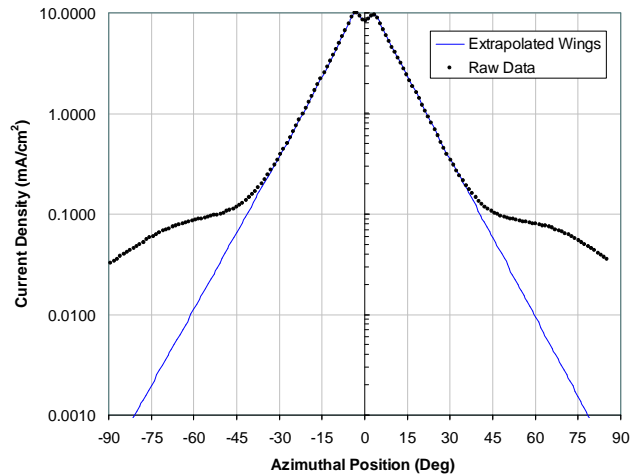


Figure 7. Current density from nude Faraday probe traces showing increased current collection on the wings due to CEX ions. Data beyond $\pm 30^\circ$ is extrapolated for charge divergence and beam current calculations.

IV. Experimental Results and Discussion

Thruster efficiency and the three utilizations are analyzed along a line of constant power (6 kW) and a line of constant anode flow rate (20 mg/s) to study the losses that dominate each mode of operation. Propellant utilization can be calculated using the experimentally determined thruster efficiency along with voltage utilization from the RPA and current utilization from the Faraday probe. The primary drawback to this approach is the error associated with integrating ion current density in the plume to calculate the current utilization. An artificially large beam current would increase current utilization and decrease propellant utilization.

The anode thruster efficiency, energy efficiency, and three utilization efficiencies are shown in Fig. 8. Propellant utilization is the driving loss mechanism for both the constant flow and constant flow rate conditions. A low propellant utilization can be attributed to low ionization fraction and/or a large momentum divergence angle.

In both plots, the voltage and current utilization are nearly equal above 200 V discharge. At discharge voltages below 200 V, the potential required for ionization becomes a significant fraction of the anode acceleration potential. This loss of available acceleration potential is seen in the reduced voltage utilization in the 20 mg/s case for 100 V and 150 V discharge.

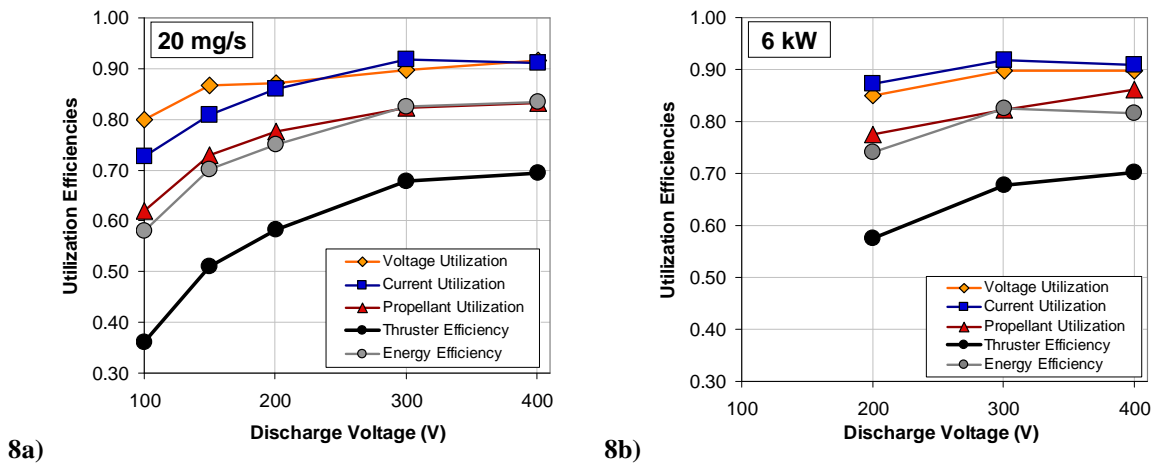


Figure 8. Thruster efficiencies for constant anode flow rate of 20 mg/s (8a) and constant power of 6 kW (8b) with increasing discharge voltage.

An inspection of the relationship between thruster efficiency, energy efficiency, and propellant utilization in Fig. 9 reveals similar linear characteristics between the lines of constant power and flow rate. Performance is predominately driven by discharge voltage as opposed to anode propellant flow rate or discharge current for discharge voltages <300 V. Propellant utilization continues to increase from 300 V to 400 V, while energy efficiency decreases for constant power and increases for constant anode mass flow operating conditions. Thruster efficiency increases in both instances. The reduction in energy efficiency is traced back to a slight decrease in current utilization from 92% to 91%. However, while voltage efficiency increases for constant mass flow, it is stable at 90% in the case of constant power. Additional experiments are required to distinguish a clear trend due to the limited data. Since discharge voltage appears to be the primary efficiency driver, further analysis will focus on variations with applied anode potential.

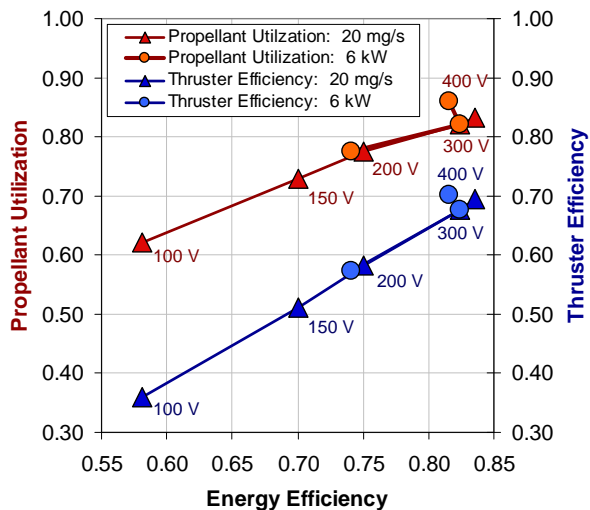


Figure 9. Relationships between propellant utilization, thruster efficiency, and energy efficiency for a line of constant anode flow (20 mg/s) and constant power (6 kW).

Incorporating thruster telemetry, performance, and far-field plume measurements into the experimental parameter groups, E_1 and E_2 , supplies two equations used to extract complimentary values for three plasma parameters. Examining permissible values for the limits of 100% ionization ($f_i=1$) and zero momentum beam divergence ($\alpha=0$, $\Phi_{VDF}=1$) provides a range of consistent values.

A range of permissible values for average particle charge can be evaluated using the limits of $f_i=1$ for the minimum Q value and zero beam divergence ($\Phi_{VDF}=1$) for the maximum Q . The traces in Fig. 10 show the range of permissible Q decreasing as discharge voltage increases for both constant flow and constant power operation. The range stabilized for the case of constant anode flow rate at $Q_{min}=1.23$ and $Q_{max}=1.45$. For constant power operation, the values of both Q_{min} and Q_{max} continue to decrease beyond 400 V discharge. Lower discharge current appears to decrease the maximum and minimum values of Q (400 V conditions), while higher current increases the limits (200 V conditions). For discharge voltages >200 V at constant mass flow operation, the average charge must be ≥ 1.23 , which implies a significant fraction of multiply charged ions in the thruster discharge.

Variations in ionization fraction with increasing discharge voltage are shown in Fig. 11, with contours of constant α from $0^\circ - 90^\circ$. The maximum ionization fraction of $f_i=1$ places limits on acceptable ion beam divergence angles for a given discharge voltage. For example, the maximum momentum divergence at 400 V, 6 kW is approximately 55° . However, this large beam divergence would correspond to 100% ionization with the minimum allowable average charge, Q . At 20 mg/s and 100 V discharge, the range of momentum beam divergence from $0^\circ - 60^\circ$ corresponds to an ionization fraction of 0.65 to 0.75. Unity ionization fraction is not possible at this operating condition, even for a 90° momentum divergence half-angle. This signifies reduced ionization is a leading loss mechanism at low discharge voltage.

The maximum momentum divergence half-angle can be examined using the values of the E_1 , $(1-\beta)$, and χ to calculate profiles for lines of constant ionization fraction, as shown in Eq. (16) and (17). For an isotropic distribution of divergences, the divergence component of the propellant utilization is the factor by which thrust of an ideal 1-dimensional rocket jet is reduced to its 2-dimensional divergence.

$$\frac{E_1}{a\chi(1-\beta)} = \Phi_{DIV} f_i \quad (16)$$

$$\Phi_{DIV} = \left(\frac{1 + \cos\alpha}{2} \right)^2 \quad (17)$$

Contours of momentum divergence half-angle for a given ionization fraction are shown in Fig. 12. Calculated divergence of the 20 mg/s conditions shown in Fig. 12a display an exponential decrease with increasing discharge voltage, and exposes high beam divergence as a leading loss mechanism at low discharge voltage. In this case, the line of $f_i=1$ places an upper limit to the momentum divergence half-angle of $<34^\circ$ at 300 V. In Fig. 11b, beam divergence profiles for constant power operation show $f_i \geq 0.88$ at 400 V discharge while $\alpha \leq 29^\circ$.

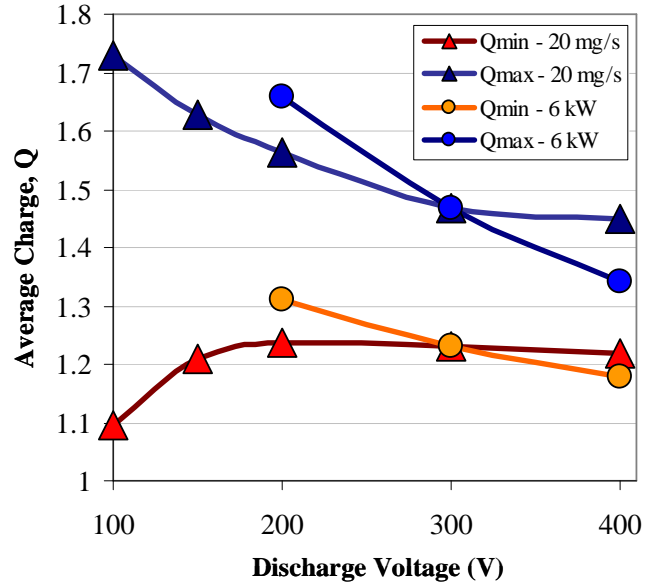


Figure 10. Range of permissible average ion charge for constant anode flow rate (20 mg/s) and constant power (6 kW) with increasing discharge voltage.

A comparison between the charge divergence calculated from current density measurements with analytically extracted contours of momentum divergence is displayed in Fig. 12. The 90% and 95% beam divergence angles calculated from Faraday probe sweeps of current density in the far-field plume are higher than the momentum divergence angle for all discharge voltages, with the exception of 90% charge divergence at 20 mg/s and 300-400 V discharge. The most likely cause of this discrepancy is the presence of low energy CEX ions on the thruster wings contributing a significant fraction to the integrated charge divergence. While extrapolation for $\pm 30^\circ$ beyond thruster centerline reduces the effects of CEX, it appears the integration may over-predict charge divergence and ion beam current from a Faraday probe scan. The primary drawback to this analysis is that an over-predicted ion beam current will artificially increase the calculated current utilization while decreasing propellant utilization, with an auxiliary effect of further decreasing the maximum momentum divergence half-angle.

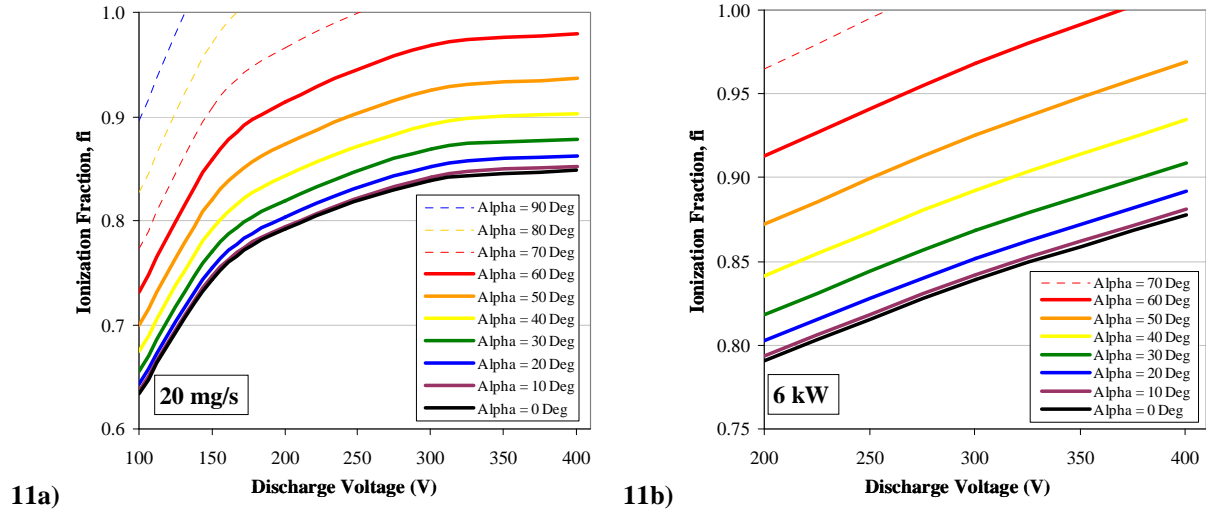


Figure 11. Ionization mass fraction for constant anode flow rate of 20 mg/s (11a) and constant power of 6 kW (11b) with increasing discharge voltage for lines of constant momentum divergence half-angle, α .

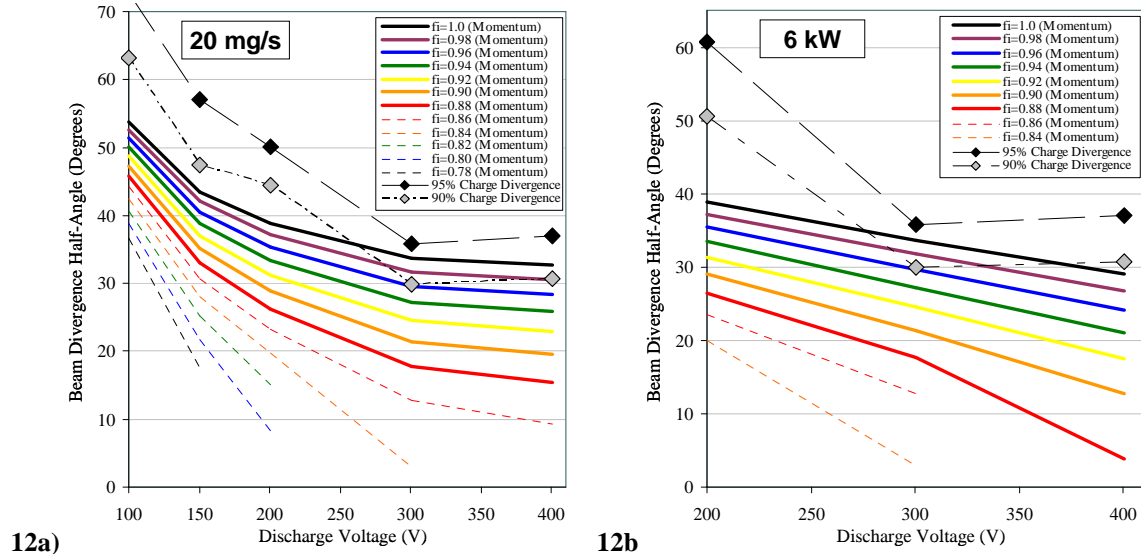


Figure 12. Comparison of measured charge divergence with profiles of calculated momentum beam divergence half-angles for constant anode flow rate of 20 mg/s (12a) and constant power of 6 kW (12b) with increasing discharge voltage for lines of constant ionization fraction.

While analyzing limits of specific terms aids in bounding acceptable parameters, bracketing more probable consistent sets of plasma properties provides enhanced knowledge of thruster operation. For data at 400 V and 6 kW, the χ -Factor is $\chi = Qf_i = 0.18$ and the quantity $\Phi_{Div,fi} = 0.88$ using Eq. (16). Using these values and the limits of each term ($Q \geq 1$, $f_i \leq 1$, $\Phi_{Div} \leq 1$), the plasma properties f_i , Q , and α are shown in Fig. 13 with a table of acceptable values. The green regions highlight more plausible conditions, where the momentum divergence is $>10^\circ$ and the ionization fraction is $\leq 95\%$. For these constraints, the range of consistent sets reduces to an ionization fraction of 90%-95%, average charge of 1.24-1.31, and a momentum beam divergence half-angle of 13° - 23° . This example illustrates the utility of the efficiency architecture for extracting plasma parameters from a limited number of macroscopic thruster measurements. All experimental measurements and calculated parameters are tabulated in Tables 1-3 of the Appendix.

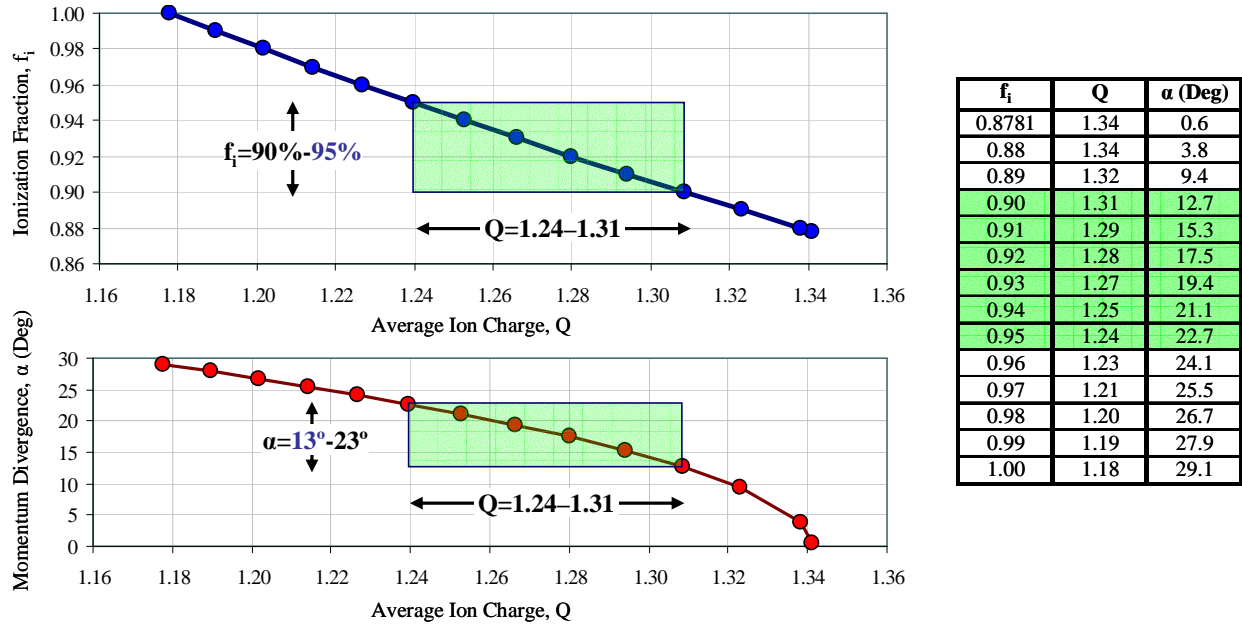


Figure 13. Consistent parameter sets of momentum divergence half-angle, average charge, and ionization fraction for 6 kW operation at 400 V discharge. Plasma properties are constrained and probable values are highlighted in green to establish a likely range of discharge characteristics.

V. Summary and Future Work

A systematic study of Hall thruster operation from 100 to 400 V discharge demonstrated the extraction of plasma properties with a limited set of macroscopic experimental measurements using an efficiency architecture developed at AFRL. The architecture analytically decomposed thrust efficiency into the product of voltage utilization, current utilization, and propellant utilization efficiency. Low ionization fraction and large momentum beam divergence were the driving loss mechanisms at low voltage for constant power and constant flow rate operation. Physical constraints on plasma properties enabled limits to be set on consistent sets of performance parameters, including the average ion charge, ionization fraction, and momentum divergence half-angle. Including ExB or LIF measurements with this technique would close the set of equations and enable the calculation of a full set of discharge parameters, including the aforementioned properties. Internal and near-field plasma potential and density measurements will be conducted to compare the theoretical effectiveness in predicting plasma properties with experimental results, and further understanding of the loss mechanisms affecting Hall thruster operation.

Appendix

Table 1: Thruster telemetry data for lines of constant mass flow (20 mg/s) and power (6 kW).

Test Point	V _D (V)	I _D (A)	P _D (A)	Mass Flow (mg/s)		Cathode Potential (V)	Background Pressure (Torr)	Thrust (mN)
				Anode	Cathode			
8	100	22	2245	20.2	1.4	-7.4	1.4E-05	181
9	150	22	3340	20.2	1.4	-9.1	1.4E-05	263
10	201	21	4289	20.2	1.4	-10.2	1.3E-05	318
11	301	20	5997	20.2	1.4	-11.6	1.2E-05	405
13	401	20	8040	20.2	1.4	-10.7	1.2E-05	475
19	400	15	6044	15.8	1.1	-13.3	9.2E-06	366
20	200	30	6031	27.3	1.9	-10.3	1.9E-05	435
21	600	10	6029	10.6	0.7	-18.1	7.1E-06	304

Table 2: Experimental Parameter Groups, Utilization Efficiencies, and Plasma Parameters (for f_i=1).

Test Point	Experimental		(1-β)	(1-r)	Φ	Thrust Efficiency	χ	For f _i = 1			
	E ₁	E ₂						Q _{min}	Φ _{VDF}	Φ _{div}	α (Deg)
8	0.54	0.66	0.80	0.73	0.62	0.36	1.10	1.10	0.99	0.63	54
9	0.76	0.67	0.87	0.81	0.73	0.51	1.21	1.21	0.99	0.74	44
10	0.84	0.70	0.87	0.86	0.78	0.58	1.24	1.24	0.99	0.78	40
11	0.91	0.75	0.90	0.92	0.82	0.68	1.23	1.23	0.99	0.83	35
13	0.94	0.74	0.92	0.91	0.83	0.69	1.23	1.23	0.99	0.84	34
19	0.91	0.77	0.90	0.91	0.86	0.70	1.18	1.18	0.99	0.87	30
20	0.86	0.66	0.85	0.87	0.77	0.57	1.31	1.31	0.99	0.78	40
21	0.93	0.78	-	-	-	-	-	-	-	-	-

Table 3: Far-field Plasma Plume Measurements at 1-meter on thruster centerline.

Test Point	Nude Faraday 95% Half-Angle		Nude Faraday 90% Half-Angle		Integrated Beam Current (A)	Plasma Potential (V)	Most Probable Ion Voltage (V)
	Avg. (deg)	± Deviation (deg)	Avg. (deg)	± Deviation (deg)			
8	72.9	1.1	63.2	1.1	16.3	8	88
9	57.1	0.9	47.4	0.8	18	12	142
10	50.1	1.0	44.4	2.2	18.4	13	188
11	35.8	3.5	29.9	2.6	18.3	14	284
13	37.0	1.4	30.7	1.7	18.3	15	382
19	37.0	1.4	30.7	1.7	13.7	17	376
20	60.6	0.5	50.6	0.4	26.3	12	182
21	40.7	2.8	33.5	2.4	10.1	-	-

Acknowledgments

The authors would like to thank Ron Watkins and Rich Hofer of JPL for their prompt assistance repairing a cathode. The maintenance on Chamber #3 at AFRL by Bob Gregory and David Skipworth during testing is gratefully acknowledged.

References

- 1 Larson, C. W., Brown, D. L., Hargus, W. A., "Thrust Efficiency, Energy Efficiency, and the Role of VDF in Hall Thruster Performance Analysis," Proceedings of the 43rd AIAA/ASME/SAE/ASEE Joint Propulsion Conference, AIAA-2007-5270, Cincinnati, OH, July 8-11, 2007.
- 2 Hofer, R. R., Gallimore, A. D., "High-Specific Impulse Hall Thrusters, Part 2: Efficiency Analysis," *Journal of Propulsion and Power*, Vol. 22, No. 4, 2006, pp. 732-740.
- 3 Hargus, W. A., Jr., Meezan, N. B., Cappelli, M. A., "The Transient Behavior of a Low Power Laboratory Xenon Hall Thruster," *Proceedings of the 33rd AIAA/ASME/ASEE Joint Propulsion Conference*, AIAA 1997-3050, Seattle, WA, July 6-9, 1997.
- 4 Randolph, T. Kim, V., Kaufman, H., Kozubsky, K., Zhurin, V., Day, M. "Facility Effects on Stationary Plasma Thruster Testing," *23rd International Electric Propulsion Conference*, IEPC-93-93, Seattle, WA, Sept 13-16, 1993.
- 5 Hofer, R. R., Peterson, P. Y., Gallimore, A. D., "Characterizing Vacuum Facility Backpressure Effects on the Performance of a Hall Thruster," *27th International Electric Propulsion Conference*, IEPC-01-045, Pasadena, CA, Oct 14-19, 2001.
- 6 Walker, M. L. R., "Effects of Facility Backpressure on the Performance and Plume of a Hall Thruster," Ph.D. Thesis, Department of Aerospace Engineering, Univ. of Michigan, Ann Arbor, MI, 2005.
- 7 Hutchinson, I. H., Principles of Plasma Diagnostics, 2nd Edition, Cambridge Univ. Press, New York, 1990.
- 8 Beal, B. E., "Clustering of Hall Effect Thrusters for High-Power Electric Propulsion Applications," Doctoral Thesis, Department of Aerospace Engineering, Univ. of Michigan, Ann Arbor, MI, 2004.
- 9 Hofer, R. R., Haas, J. M., Gallimore, A. D., "Ion Voltage Diagnostics in the Far-Field Plume of a High-Specific Impulse Hall Thruster," *Proceedings of the 39th AIAA/ASME/ASEE Joint Propulsion Conference*, AIAA 2003-4556, Huntsville, AL, July 20-23, 2003.
- 10 Gulszinski, F. S., "Examination of the Structure and Evolution of Ion Energy Properties of a 5 kW Class Laboratory Hall Effect Thruster at Various Operational Conditions," Doctoral Thesis, Department of Aerospace Engineering, Univ. of Michigan, Ann Arbor, MI, 1999.
- 11 Walker, M. L. R., Hofer, R. R., Gallimore, A. D., "Ion Collection in Hall Thruster Plumes," *Journal of Propulsion and Power*, Vol. 22, No. 1, 2006, pp. 205-209.
- 12 Manzella, D. H., Sankovic, J. M., "Hall Thruster Ion Beam Characterization," NASA TM-107034, Aug. 1995.
- 13 Boyd, I. D., "Review of Hall Thruster Plume Modeling," *Journal of Spacecraft and Rockets*, Vol. 38, No. 3, 2001, pp. 381-387.
- 14 Hofer, R. R., Walker, M. L. R., Gallimore, A. D., "A Comparison of Nude and Collimated Faraday Probes for Use with Hall Thrusters," IEPC-01-020, 27th International Electric Propulsion Conference, Pasadena, CA, Oct 14-19, 2001.
- 15 McVey, J. B., Britt, E. J., Engelman, S. F., Gulszinski, F. S., Beiting, E. D., Pollard, J. E., "Characteristics of the T-220HT Hall-Effect Thruster," Proceedings of the 39th AIAA/ASME/ASEE Joint Propulsion Conference, AIAA 2003-5158, Huntsville, AL, July 20-23, 2003.